MAGNETOHYDRODYNAMICS Vol. 59 (2023), No. 3-4, pp. 315–331
DOI: 10.22364/mhd.59.3-4.5

INFLUENCE OF INLET SWIRL ANGLE ON ALKALI METAL SEED MIXING EFFECT OF INERT GAS DISK MHD GENERATOR

Peiqi Zhu [1,2], *Aiwu Peng* [1,2]

[1] *University of Chinese Academy of Sciences, Beijing 100049, China*
[2] *Institute of Electrical Engineering, Chinese Academy of Sciences, Beijing 100190, China*
e-Mail: zhupeiqi@mail.iee.ac.cn, pengyan@mail.iee.ac.cn

For the high temperature plasma disk MHD generator test device, the Institute of Electrical Engineering, Chinese Academy of Sciences proposed an accurate and stable injection system of alkali metal seeds based on a pneumatic atomization nozzle, which can realize the quantitative delivery of seed flow to the upstream mixing chamber of the generator on demand, vaporize the seeds through the heat transfer between the high enthalpy inert gas and alkali metal seeds, and evenly mix the seed jet with the main inert gas flow. In this paper, the mixing process of alkali metal seeds injected by the pneumatic atomizing nozzle and high-temperature argon in the upstream and inside the generator is numerically simulated. Under typical working conditions, the effects of different inlet swirl angles on the mixing effect of alkali metal seeds were simulated and analyzed when four spray guns were evenly distributed. The spatial distribution and variation of the seed fraction in the disc channel were emphatically analyzed. The uniformity of seeds in the effective section of the channel was evaluated by calculating the non-uniformity coefficient of gaseous cesium. The plasma ionization characteristics of the anode inlet of the power generation channel were also evaluated. The results show that the increase of the swirl angle at the inlet has a negative impact on the seed fraction level of the power generation channel. The plasma conductivity distribution at the anode inlet is related to the spatial distribution of seeds. Under the condition of inlet swirl, the total electron number density at the anode inlet will decrease by about 2–3 orders of magnitude.

Introduction.

Magnetohydrodynamic (MHD) power generation is a power generation method that uses electromagnetic induction between a moving conducting fluid and an orthogonal magnetic field to generate current at both ends of the electrodes. It has broad prospects in clean energy power generation and space power supply. According to the different properties of the conducting fluid, MHD power generation can be divided into coal-fired MHD power generation, liquid metal MHD power generation and inert gas plasma MHD power generation, etc. The inert gas plasma MHD is driven by a high-temperature heat source. The heat source heating and self-excited Joule heat cause the inert gas to ionize and form plasma. The plasma cuts the magnetic field at a high speed and generates electrical energy output at both ends of the electrode. This power generation method has high power density, high efficiency, and other advantages [4, 6].

Since pure inert gas elements are ionized under the temperature and pressure conditions of conventional heat sources, even in non-equilibrium ionization, the conductivity is at a low level (<1 S/m). Therefore, the conductivity of inert gas plasma needs to be improved to meet power generation requirements. A common method is to dope the inert gas carrier with a trace amount of an element with a low ionization potential, which is also called a power generation seed. At present, the optional inert gas carrier is generally argon or helium [3], and the power generation seeds are alkali metals, such as cesium, potassium, rubidium, and gases, such as xenon. Generally, alkali metal seeds have the lowest ionization potential, so they produce the best power generation results. The common high-power MHD generator is of disk configuration. The MHD generator uses a

mixture of inert gas and alkali metal seeds as the power generation working fluid to generate non-equilibrium plasma in the annular power generation channel. The conductivity can reach hundreds of S/m [5].

For the high-temperature plasma disk MHD generator test device, the Institute of Electrical Engineering of the Chinese Academy of Sciences has developed a precise and stable alkali metal seed injection system based on a pneumatic atomization nozzle, which can realize quantitative delivery of the seed flow to the upstream of the generator on demand. In the mixing chamber, the seeds are vaporized through the heat transfer between the high-enthalpy inert gas and the alkali metal seeds, and at the same time, the seed jet is evenly mixed with the main flow of the inert gas. The precise and stable seed injection system includes all operable subsystems, such as alkali metal transportation pipelines, inert gas transportation pipelines, pneumatic atomization spray guns, data acquisition modules, host computer monitoring system and thermal management system, etc.

The effect of mixing alkali metal seeds with inert gases has a significant impact on the performance of generators. Due to the uneven spatial distribution of seeds during mixing, it can cause an uneven and unstable plasma in the power generation channel [1]. At the same time, too large or too small seed fractions can lead to inefficient power generation in disk generators [2]. Therefore, it is necessary to conduct a numerical simulation on the mixing process of alkali metal seeds and inert gases in the generator.

In this paper, the mixing process of alkali metal seeds and high-temperature argon injected by the pneumatic atomizing nozzle upstream and inside of the generator is numerically simulated. The seed distribution in the main channel under different inlet swirl angles is analyzed, and the non-uniformity coefficient of gaseous cesium is proposed to measure the seed distribution. At the same time, the ionization characteristics of equilibrium plasma are analyzed. This provides a reference for the optimization of the seed fraction control method of the inert gas plasma MHD generator in the future.

1. Physical models and numerical program.

A three-dimensional physical model of numerical simulation is shown in Fig. 1, including a heat source, an alkali metal seed injection ring, a mixing section, a variable diameter section, a measurement section, and a disk generator. The shape and structural dimensions of the channel are shown in Fig. 2.

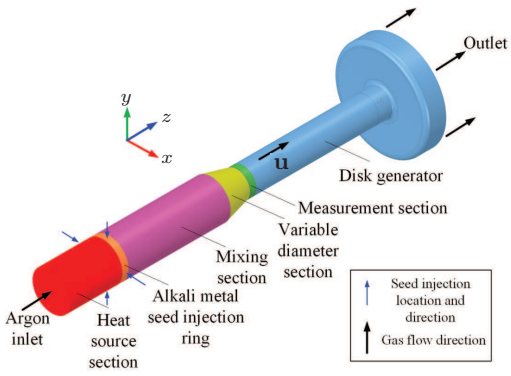

Fig. 1. The three-dimensional physical model of the main channel of the disk generator.

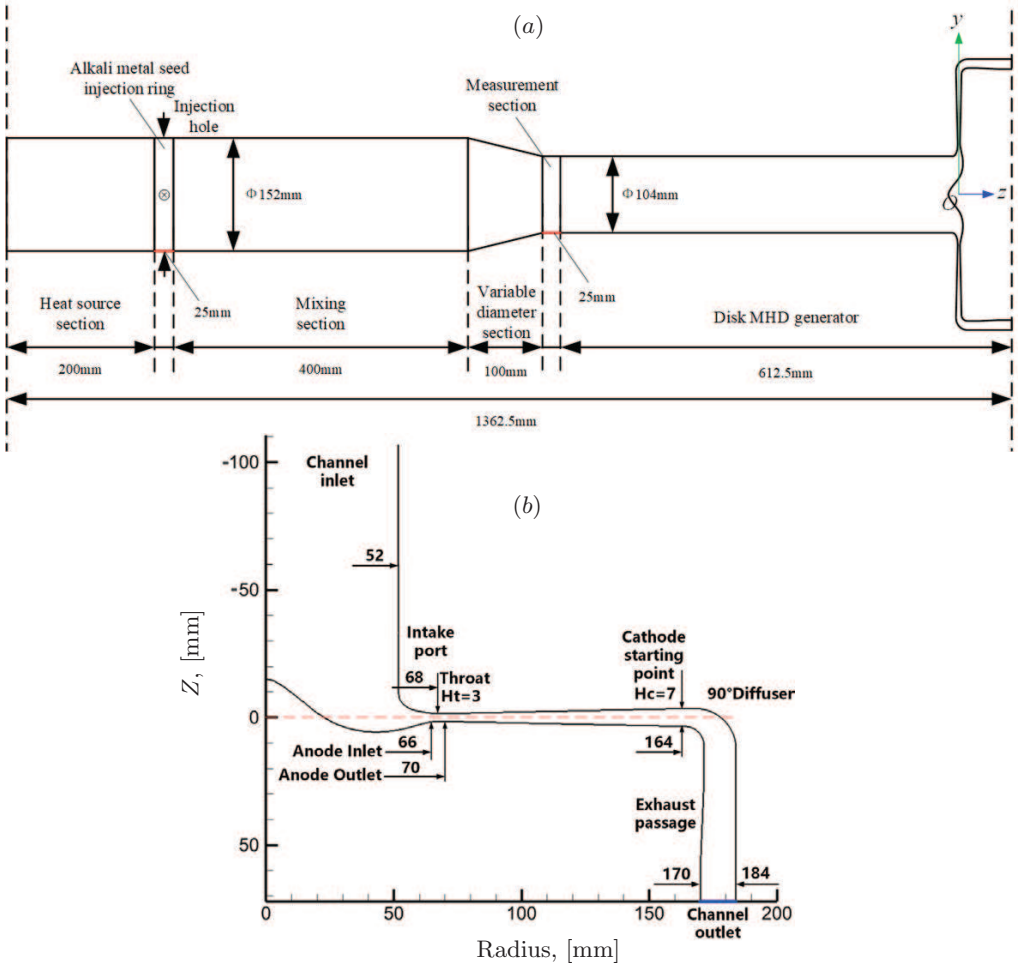

Fig. 2. Shape and structural parameters of the main channel of the disk MHD generator. (*a*) Overall schematic. (*b*) Generator overall structure.

The coordinate system is assumed with the central plane of the effective section of the generator as $Z = 0$, and the range of the Z-direction of the disk generator is [–540.5 mm, 72.0 mm]. The generator is a typical supersonic diffusion flow channel, the throat height $H_t = 3$ mm, the cathode starting point height $H_c = 7$ mm, and the gas diffusion area ratio $A_R = 5.63$. The anode radius range is 66–70 mm, and the starting radius of the cathode is 164 mm. The alkali metal seed injection ring has four injection holes uniformly distributed in the circumferential direction and vertically inward along the radial direction. There are two positions of the injection holes on the X-axis and two on the Y-axis. The Z-coordinates corresponding to the four injection holes are all –1078 mm.

The numerical simulation program used in this study is based on fluid dynamics, a component transport model and a discrete phase model, and mainly adopts the following assumptions.

(1) The numerical simulation is aimed at a long-term steady-state flow of gas. The main operating parameters, such as the total inlet temperature, total inlet pressure, and wall temperature are kept constant over time, and gravity is ignored.

(2) The injection of alkali metal seeds realized by the spray gun is assumed as a uniform steady-state conical jet. The jet is injected from a small circle with a diameter of ∅0.4 mm centered in the injection hole. The initial parameters of the jet, such as the atomization shape, atomization particle size, atomization angle, liquid mass flow rate, initial injection velocity of droplets, droplet temperature, etc., remain constant over time.

(3) The mixed gas and its components are considered to be ideal gases, and the heating caused by the viscous dissipation of the gas is ignored.

(4) Liquid cesium particles are assumed to be spherical particles with a uniform temperature and density, and the initial particle size of cesium particles is single and uniform.

To meet the accuracy of high-speed flow simulation, we adopt the realizable *k-varepsilon* model to describe turbulence. Structured grid partitioning was made for the fluid domain, and three different sizes of grids were drawn: 4.5 million, 8.2 million, and 12 million. The grid independence was tested, and it was confirmed that the current grid (8.2 million) is close to achieving a balance between computational speed and accuracy. By using explicit time stepping, the continuous phase flow equations, component transport equations, and discrete phase particle equations are solved alternately at each time step. When the residual values of all the variables in the equation set are less than 10^{-3}, the convergent flow field is obtained.

1.1. Flow model. The behavior of argon-cesium gas mixtures in the mainstream can be expressed by the 3D viscous compressible Navier–Stokes equations.

The continuity equation,

$$\frac{\partial \rho}{\partial t} + \nabla \cdot (\rho \mathbf{u}) = S_{\mathrm{m}}, \tag{1}$$

where ρ is the density of the mixed gas, S_{m} is the mass exchange between liquid cesium particles and gas.

The momentum equation,

$$\frac{\partial}{\partial t}(\rho \mathbf{u}) + \nabla \cdot (\rho \mathbf{u}\mathbf{u}) = -\nabla p + \nabla \cdot \overline{\tau} + \mathbf{F}_{\mathrm{p}}, \tag{2}$$

where $\mathbf{F}_{\mathrm{p}}$ is the momentum exchange between liquid cesium particles and gas.

The energy equation,

$$\frac{\partial}{\partial t}(\rho E) + \nabla \cdot (\mathbf{u}(\rho E + p)) = \nabla \cdot \left(k_{\mathrm{eff}} \nabla T - \sum_j h_j \mathbf{J}_j \right) - Q, \tag{3}$$

with E being the total energy of the gas substance, k_{eff} the mass diffusion coefficient of cesium in the mixture, h_j is the apparent enthalpy of gaseous cesium/argon gas, $\mathbf{J}_j$ is the component diffusion flux, and Q is the heat exchange between liquid cesium particles and gas.

1.2. Turbulence model. In this paper, the realizable *k-varepsilon* two-equation turbulence model is used, and the turbulent viscosity is calculated according to the turbulent energy k and the dissipation rate ε:

$$\frac{\partial}{\partial t}(\rho k) + \frac{\partial}{\partial x_j}(\rho k u_j) = \frac{\partial}{\partial x_j}\left[\left(\mu + \frac{\mu_t}{\sigma_k} \right) \frac{\partial k}{\partial x_j} \right] + G_{\mathrm{k}} - \rho \varepsilon - Y_M, \tag{4}$$

$$\frac{\partial}{\partial t}(\rho\varepsilon)+\frac{\partial}{\partial x_j}(\rho\varepsilon u_j)=\frac{\partial}{\partial x_j}\left[\left(\mu+\frac{\mu_t}{\sigma_\varepsilon}\right)\frac{\partial\varepsilon}{\partial x_j}\right]+\rho C_1 S\varepsilon-\rho C_2\frac{\varepsilon^2}{k+\sqrt{v\varepsilon}}+C_{1\varepsilon}\frac{\varepsilon}{k}C_{3\varepsilon}G_b, \quad (5)$$

where G_k stands for the turbulent kinetic energy due to the average velocity gradient, Y_M characterizes the effect of expansion dissipation in compressible turbulent flow on the turbulent flow, σ_k and σ_ε are the turbulent Prandtl numbers of k and ε, respectively, and C_2 and $C_{1\varepsilon}$ are constants.

1.3. Component transport model.

$$\frac{\partial}{\partial t}(\rho Y_{Cs})+\nabla\cdot(\rho\mathbf{u}Y_{Cs})=-\nabla\cdot\mathbf{J}_{Cs}+S_m, \quad (6)$$

where Y_{Cs} is the local mass fraction of gaseous cesium, J_{Cs} is the diffusion flux of gaseous cesium, which is produced by the concentration and temperature gradient, S_m is the rate of cesium phase transition to gaseous cesium.

Since the mixed gas is a two-component gas, the total mass fraction of the two components is 100%, with argon accounting for the majority. Therefore, only a component with a relatively small mass fraction, namely gaseous cesium, is required. The mass fraction of argon can be considered as 1 minus the mass fraction of gaseous cesium.

For the diffusion of gaseous cesium in turbulence, there is the following equation:

$$\mathbf{J}_{Cs}=-\left(\rho D_{Cs,m}+\frac{\mu_t}{Sc_t}\right)\nabla Y_{Cs}-D_{T,Cs}\frac{\nabla T}{T}, \quad (7)$$

where $D_{Cs,m}$ is the mass diffusion coefficient of cesium in the mixture, $D_{T,Cs}$ is the thermal diffusion coefficient, Sc_t is the turbulent Schmidt number number, μ_t is the turbulent viscosity; $Sc_t=0.7$ is assumed in this model.

1.4. Discrete phase model. The heat transfer, mass transfer, and particle size change of cesium droplet particles follow the three laws,

$$m_\mathrm{p}c_\mathrm{p}\frac{dT_\mathrm{p}}{dt}=hA_\mathrm{p}(T_\infty-T_\mathrm{p})-\frac{dm_\mathrm{p}}{dt}h_{fg}, \quad (8)$$

$$\frac{dm_\mathrm{p}}{dt}=k_cA_\mathrm{p}\rho\ln(1+B_m), \quad (9)$$

$$\frac{d(d_\mathrm{p})}{dt}=\frac{2k_\infty}{\rho_\mathrm{p}c_{p\infty}d_\mathrm{p}}\left(2+0.6\mathrm{Re}^{1/2}\mathrm{Pr}^{1/3}\right)\ln\left(1+\frac{c_{p\infty}(T_\infty-T_\mathrm{p})}{h_{fg}}\right), \quad (10)$$

where m_p is the particle mass, C_p is the particle heat capacity, T_p is the particle temperature, h is the convection heat transfer coefficient, A_p is the surface area of the particle, T_∞ is the temperature of the local continuous phase, h_{fg} denotes latent heat, k_c is the mass transfer coefficient, ρ is the gas density, B_m is the Spalding mass number, d_p is the particle diameter, k_∞ is the thermal conductivity of the gas, $C_{\mathrm{p}\infty}$ is the specific heat of the gas, Re is the Reynolds number, and Pr is the Prandtl number of the continuous phase.

1.5. Boundary conditions. For the solution of the continuous phase, the inlet of the main channel is a fixed total temperature and total pressure inlet boundary condition, and the outlet of the main channel is a pressure outlet boundary condition. The wall surface is uniformly considered as a fixed wall temperature wall surface without slip.

The velocity at the inlet has an axial component u_axial and a tangential component u_tang. u_axial and u_tang have a certain angle, which is the inlet swirl angle θ, defined as

$$\theta=\arctan\left|\frac{u_\mathrm{tang}}{u_\mathrm{axial}}\right|. \quad (11)$$

The direction of the inlet swirl flow used in this model is uniform: viewed from the positive direction of the Z-axis, the inlet swirl flow runs counterclockwise.

For the solution of the discrete phase, the liquid cesium jet is injected from a small circle with a diameter of ∅0.4 mm centered in the injection hole. Liquid cesium particles escape boundary conditions at both the inlet and the outlet of the main channel. Liquid cesium particles form a liquid film and adhere to the wall.

2. Results and discussion.

2.1. Effect of inlet swirl flow on liquid cesium gasification. When the heat source parameters are constant, the simulation analyzes the influence of different inlet swirl angles on the gasification process of liquid cesium when the four spray guns are evenly distributed. Downstream the alkali metal seed injection ring, the mixing chamber, the variable diameter section, the measuring section, and the generator inlet are arranged in sequence along the positive Z-axis direction. Since the velocity of the argon gas in this part is low and the temperature is high, the above structure is the most important occasion for gasification and phase change of alkali metal seeds. The research variable selects the volume average seed mole fraction of the mixed gas , and selects the channel cross-section of $Z = -1.1$, –1.0, –0.9, …, –0.1, –0.06, 0 m as a typical cross-section, and calculates the average seed mole fraction of the gas at the cross-section according to the following formula (the calculation results are shown in Fig. 3):

$$sf_{\text{avg}} = \frac{\int sf \cdot dS}{\int dS}. \tag{12}$$

It can be seen that when the inlet swirl angle $\theta = 0°$, the average seed mole fraction increases approximately linearly along the positive direction of the Z-axis upstream the inlet. This is because the inlet swirl angle does not exist when , and the cesium droplets flow in the positive direction of the Z-axis near the center flow of the main channel after injection. When there is an inlet swirl flow, due to the high density of the cesium droplets,

Table 1. Numerical simulation conditions – continuous phase.

Parametr	Value
Mainstream inlet total temperature, [K]	2200
Mainstream inlet total pressure, [Pa]	405300
Mainstream outlet back pressure, [Pa]	5000
Mainstream wall temperature, [K]	600
Mainstream working fluid	Argon
Mainstream entrance seed fraction, $\times 10^{-4}$	0.0

Table 2. Numerical simulation conditions – discrete phase.

Parametr	Value
Injection hole center coordinates (X, Y, Z), mm	(±76, 0, –1078), (0, ±76, –1078)
Injection direction unit normal vector, [mm]	(∓1, 0, 0), (0, ∓1, 0)
Atomized particle size, [mm]	50
Atomizing cone half cone angle, [°[	45
Initial velocity of droplets, [m/s]	50
Total volume flow rate of spray gun (4 pieces), [mL/min]	60
Inlet swirl angle, [degree]	0, 15, 30, 45, 60, 75

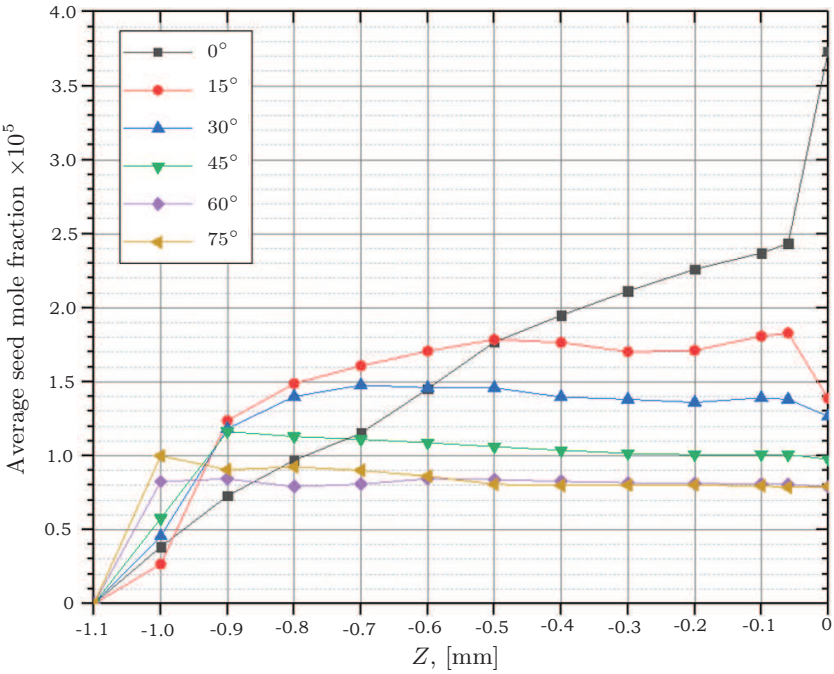

Fig. 3. Variations of the average seed mole fraction in the flow channel along the Z-axis ($\theta = 0°$, 15°, 30°, 45°, 60°, 75°).

centrifugation occurs during the movement. The cesium droplets flow tangentially to the inner wall of the channel and are captured by the wall to form a liquid film. The vaporization rate of the cesium droplets greatly decreases. As the inlet swirl angle θ increases, the cesium droplets will fly toward the inner wall faster and more concentrated, which results in the accumulation of the cesium droplets on the wall at $Z = [-1.0, -0.9]$ m, and also explains the sudden increase in the average seed mole fraction in the flow channel around $Z = -1.0$ m. The larger the inlet swirl angle θ, the more concentrated the accumulation of cesium droplets, and the smaller the sudden increase range of sf_{avg}. Since most of the cesium droplets are captured by the upstream wall, the accumulated amount of cesium on the downstream wall is very small, the growth of gaseous cesium content tends to stagnate, and sf_{avg} remains basically stable downstream the channel.

2.2. Spatial distribution of the gaseous cesium seed fraction and assessment of cesium uniformity under the influence of inlet swirl flow. The spatial distribution of the seed mole fraction of gaseous cesium in the $Y = 0$ plane under different inlet swirl angles is shown in Fig. 4. It is seen that when there is no inlet swirl ($\theta = 0°$), the mole fraction of gaseous cesium seeds is lower than 5×10^{-5} near the upstream wall of the power generation channel and close to 1×10^{-4} near the central flow because the cesium droplets gather in the center of the argon gas and flow downstream. The high-temperature argon gas in the center flow vaporizes the cesium droplets and mixes with the argon gas. Some cesium droplets accumulate at the bottom of the inlet cone upstream the throat, causing the mole fraction of gaseous cesium seeds there to be higher than 4×10^{-4}. However, due to the low flow velocity here, the gaseous cesium is difficult to be transported to the effective section of the power generation channel. In the effective section of the power

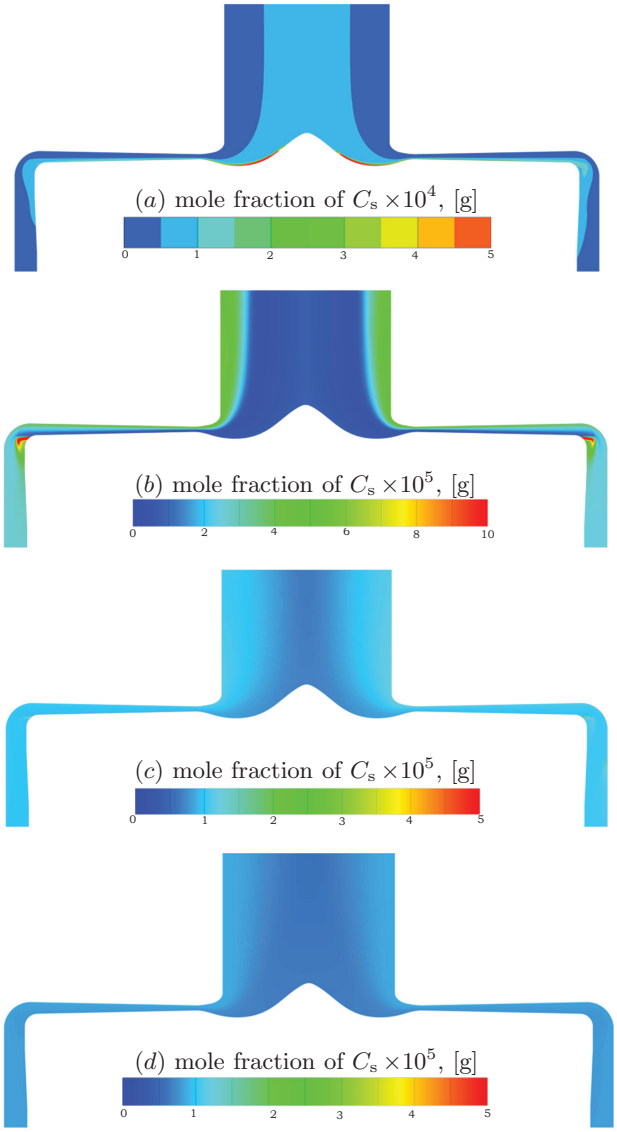

Fig. 4. Distribution of the seed mole fraction in the $Y = 0$ plane under different swirl angles: (*a*) $\theta = 0°$, (*b*) $\theta = 15$, (*c*) $\theta = 45°$, (*d*) $\theta = 75°$.

generation channel, the seed fraction shows a "low level with a negative z value and a high level with a positive z value" distribution because the seed fraction distribution is controlled by the direction of the gas flow. Comparing with Fig. 5 shows that the seed fraction distribution is consistent with the direction of the streamline. When the inlet swirl angle is small ($\theta = 15°$), most of the cesium droplets condense on the upstream wall of the channel, resulting in a higher seed fraction near the upstream wall of the channel ($> 4 \times 10^{-5}$), while the seed fraction near the central flow is lower ($< 1 \times 10^{-5}$). In the boundary layer separation region near the cathode, the gaseous cesium seeds accumulate more, so the seed fraction is higher (1×10^{-4}). In the effective section of the power

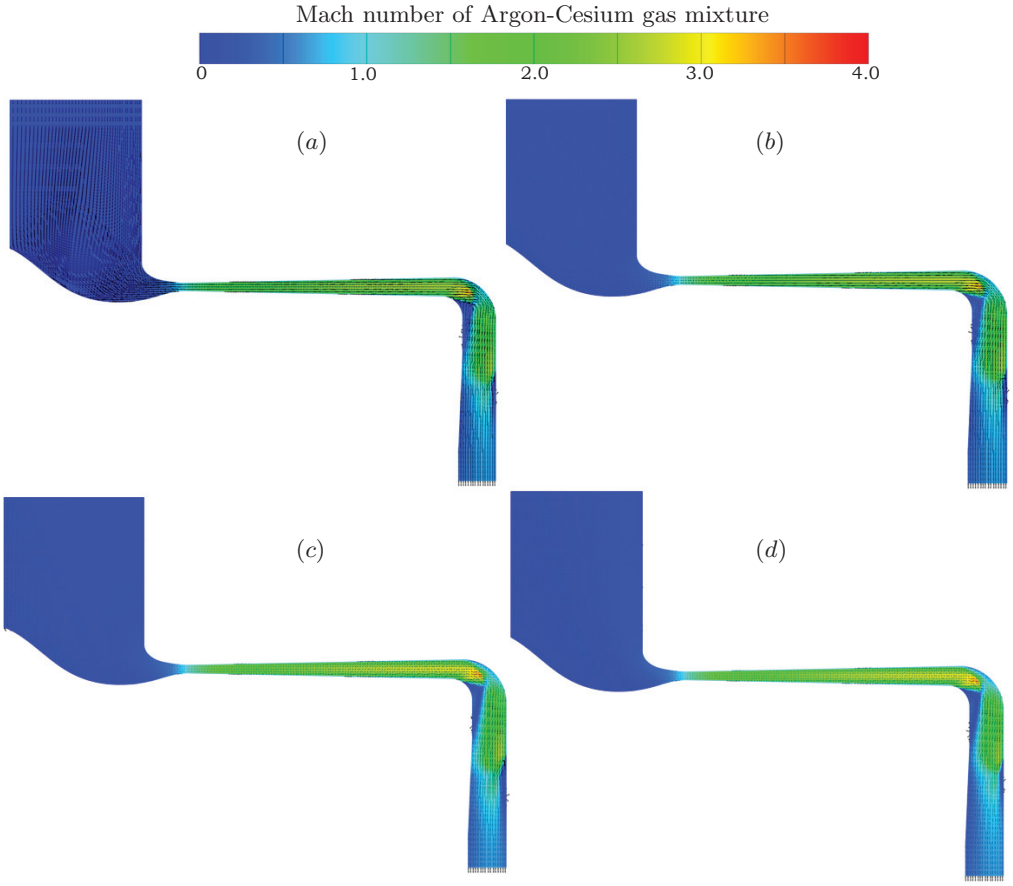

Fig. 5. Distribution of the gas Mach number and streamlines in the $Y = 0$ plane under different swirl angles: (*a*) $\theta = 0°$, (*b*) $\theta = 15°$, (*c*) $\theta = 45°$, (*d*) $\theta = 75°$.

generation channel, the seed fraction shows a "high level with a negative z value and a low level with a positive z value" distribution. When the inlet swirl angle is large ($\theta = 75°$), the cesium droplets condense on the wall near the pneumatic atomization spray gun, resulting in a generally small seed fraction upstream the channel (1×10^{-5}). In the effective section of the power generation channel, the seed fraction presents a relatively uniform and low-level (1×10^{-5}) distribution along the positive Z-direction and the radius direction.

The gaseous power generation working fluid enters the effective section of the power generation channel and flows radially, after being shaped by the flow pattern of the generator inlet and conical flow channel. The uniformity of the seed fraction of the gaseous power generation working fluid directly affects the uniformity and stability of the plasma, which in turn affects the power generation power and efficiency of the disk MHD generator. Under the influence of the inlet swirl flow, the cesium seeds show uneven distribution characteristics after entering the power generation channel section. In order to characterize the uneven degree of the seed fraction, an uneven coefficient of the gaseous cesium seed fraction is introduced by analogy with the uneven coefficients of

temperature and flow field.

The uneven coefficient of gaseous cesium seed fraction in the effective section of the power generation channel is

$$r_{sf} = \frac{\sqrt{\frac{1}{n}\sum_{i=1}^{n}(sf_i - \overline{sf})^2}}{\overline{sf}}, \tag{13}$$

where n is the number of monitoring points in the effective section of the power generation channel, $\overline{sf}$ is the average seed fraction of the monitoring points, sf_i is the local seed fraction of the monitoring point.

The coordinates of the monitoring points are selected in the following way: the monitoring points are based on the origin of the coordinate system and are 20 mm apart in the X- and Y-directions, and 1 mm apart in the Z-direction. The points of the three-dimensional lattice with a total number of 910 arranged in this way inside the effective section of the power generation channel become monitoring points. After interpolating the seed scores of these monitoring points in the simulation results, they are calculated using the uneven coefficient calculation formula. The calculation results are summarized in Table 3.

It is seen that the uneven coefficient of the gaseous cesium seed fraction in the effective section of the power generation channel decreases significantly with the increase of the inlet swirl angle. With a large inlet swirl angle ($\theta > 45°$), the uneven coefficient of the gaseous cesium seed fraction is below 0.05, indicating that the distribution of gaseous cesium in argon is relatively uniform, evidencing that the increase of the inlet swirl angle can improve the mixing effect of gaseous cesium and argon to a certain extent.

2.3. Assessment of wall adhesion of liquid cesium seeds. Fig. 6 shows the spatial distribution and particle size of the cesium droplets sprayed by a single spray gun (injection hole coordinates: –0.076, 0, –1.078 m) under different swirl angles. The initial diameter of the cesium droplets is 50 μm. It is seen that when $\theta = 0°$, there is no swirling effect at the inlet. Therefore, under the action of the radial outlet velocity and the axial main gas flow, the cesium droplets are relatively concentrated and ejected into the main gas flow and subject to the friction and shear force of the main gas flow. As a result, the radial exit velocity gradually decreases, and the axial velocity gradually increases until it flows with the main gas flow and the cesium droplets do not adhere to the wall. When $\theta > 0°$, due to the effect of the inlet swirl flow, the distribution of cesium droplets demonstrates typical spiral characteristics. After the cesium droplets are ejected from the spray gun, they distribute in an oblique cone shape in the Z-axis positive direction.

Table 3. The uneven coefficient of gaseous cesium seed fraction in the effective section of the power generation channel changes with the inlet swirl angle θ.

Inlet swirl angle θ, [degree]	Non-uniformity coefficient of gaseous cesium seed fraction
0	0.8928
15	0.6203
30	0.1634
45	0.0438
60	0.0232
75	0.0257

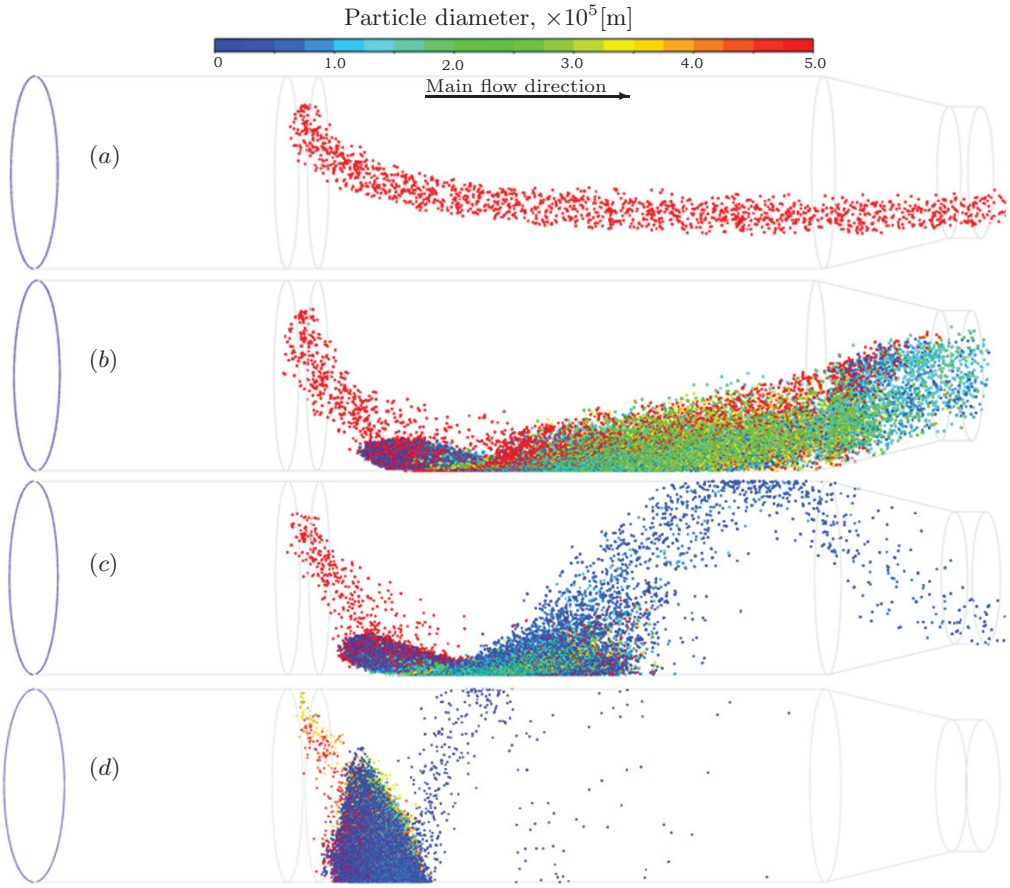

Fig. 6. Spatial distribution and particle size of cesium droplets sprayed by a single spray gun under different swirl angles: (*a*) $\theta = 0^\circ$, (*b*) $\theta = 15^\circ$, (*c*) $\theta = 45^\circ$, (*d*) $\theta = 75^\circ$.

Due to the high density of the cesium droplets under the action of the swirling flow, the centripetal force is not enough to maintain the tangential rotation of the droplets themselves, and the droplets are thrown away onto the flow channel wall. Due to the dispersion of the initial velocity direction of the droplets, the droplets captured by the wall will form a spiral strip of certain width. The larger the inlet swirl angle, the more concentrated the distribution of droplets on the wall surface, the smaller the pitch and the narrower the width of the spiral strip.

As to the particle size of the cesium droplets, when there is no swirl flow at the inlet, the cesium droplets quickly flow downstream the flow channel in the main gas flow. Due to the high velocity and short residence time, the vaporization of the cesium droplets is not obvious. The particle size decreases to a smaller extent. When there is a swirling flow at the inlet, most of the cesium droplets will be captured by the wall and stop flowing. They will stay on the wall for a long time. Therefore, the cesium droplets will obviously vaporize, and the particle size will greatly decrease and at different times. The cesium droplets attached to the wall showed noticeable differences in particle size.

2.4. Analysis of seed ionization characteristics at the power generation channel inlet.

During the operation of the disk MHD generator, a non-equilibrium ionization process of Ar-Cs plasma occurs in the effective section inside the power generation channel. However, the current cannot be drawn before the entrance of the effective section (i.e. the anode entrance), and only the equilibrium ionization process of Ar-Cs plasma occurs. Therefore, the seed ionization state at the anode inlet becomes an important boundary condition for analyzing the non-equilibrium ionization process in the effective section.

The electron thermal effect caused by the Faraday current before the anode entrance of the power generation channel can be considered as local thermal equilibrium ionization. According to the Saha equilibrium equation, the equilibrium ionization equation of Ar-Cs plasma can be written as

$$n_e \frac{n_{Ar^+}}{n_{Ar}} = \frac{(2\pi m_e kT)^{3/2}}{h^3} \cdot 2 \frac{g_{Ar^+}}{g_{Ar}} \cdot \exp\left(\frac{-\varepsilon_{Ar}}{kT}\right), \tag{14}$$

$$n_e \frac{n_{Cs^+}}{n_{Cs}} = \frac{(2\pi m_e kT)^{3/2}}{h^3} \cdot 2 \frac{g_{Cs^+}}{g_{Cs}} \cdot \exp\left(\frac{-\varepsilon_{Cs}}{kT}\right) \tag{15}$$

where $h = 6.624 \times 10^{-34}$ J·s, T is the plasma equilibrium temperature, ε_{Ar}, ε_{Cs} are the first ionization energies of Ar and Cs atoms, respectively, g_{Ar^+}, g_{Ar}, g_{Cs^+}, g_{Cs} are the ground state statistical weights of each particle, respectively.

The conductivity of the working fluid in the effective section of the power generation channel reads as

$$\sigma_e = \frac{n_e e^2}{m_e \overline{\nu}_{eH}}, \tag{16}$$

where m_e is the electron mass, $\overline{\nu}_{eH}$ is the average collision frequency of heavy particles-electrons.

After calculation, the change of the logarithm of the electron density n_e at the channel anode inlet under different inlet swirl angles along the Z-direction is presented in Fig. 7. At the inlet swirl angle $\theta = 0°$, n_e first increases and then decreases sharply, maintaining a high level in the mainstream. The maximum value of n_e is obtained at $Z = 0.9$ mm, which is about $10^{17}/\text{m}^3$. When the inlet swirl angle $\theta = [15°,75°]$, n_e in the main flow first increases and then decreases along the positive Z-direction. The changing trends of n_e are similar under different inlet swirl angles. The maximum value of n_e is obtained at $Z = -0.8$ mm, which is approximately $[10^{14.5},10^{16}]\,\text{m}^{-3}$. It is seen that n_e under at $\theta = 0°$ is significantly different from other working conditions because when there is no inlet swirl, the wall sticking phenomenon of seeds in the upstream of the power generation channel is weak, and the cesium vapor can always enter the power generation channel, making the seed fraction at the anode entrance large and the electron density correspondingly high. When the inlet swirl angle $\theta = [15°,75°]$, the seed fraction at the anode inlet is smaller, so the electron density is smaller.

The variation of the working fluid conductivity at the channel anode inlet along the Z-direction under different inlet swirl angles is shown in Fig. 8. At $\theta = 0°$, the conductivity first increases and then decreases, maintaining a high level at the positive half-axis of Z. The maximum conductivity is obtained at $Z = 0.9$ mm, which is about 1.29 S/m. When $\theta = [15°,75°]$, the conductivity first increases and then decreases along the positive Z-direction. The changing trends of the electrical conductivity under different inlet swirl angles are similar, with the maximum value obtained at $Z = -0.8$ mm, all below 0.15 S/m. It is seen that the conductivity under at $\theta = 0°$ is significantly different from the other working conditions, and the reason is the same as with the electron density n_e.

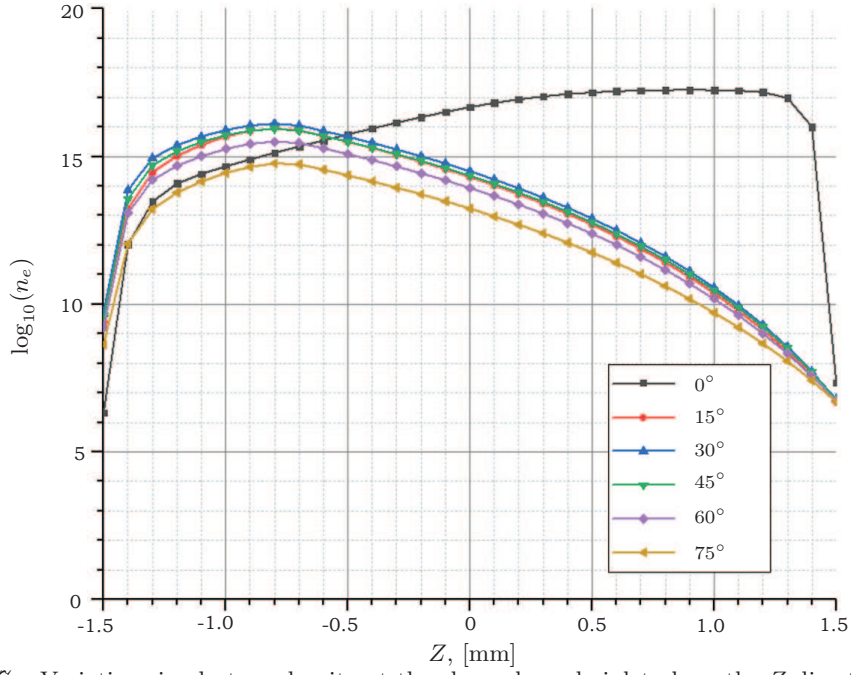

Fig. 7. Variations in electron density at the channel anode inlet along the Z-direction under different inlet swirl angles.

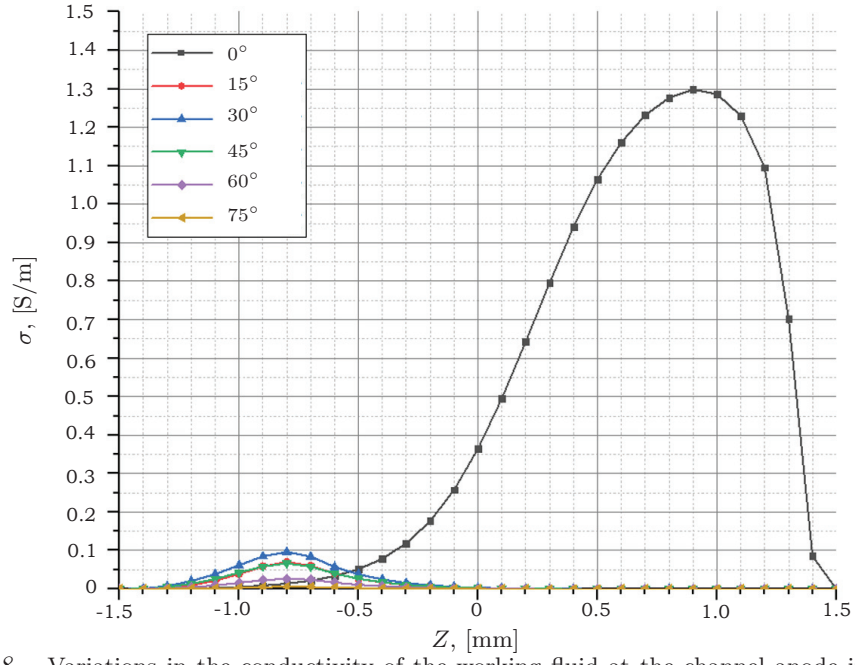

Fig. 8. Variations in the conductivity of the working fluid at the channel anode inlet along the Z-direction at different inlet swirl angles.

2.5. Remark concerning the magnetic field action. In the actual power generation process, the application of an external magnetic field will generate a tangential Faraday current density inside the plasma, which will then generate an electromagnetic force in the radial direction, hindering the plasma flow in the power generation channel, and the seed distribution of the generator will change. In particular, there are the following two working modes.

(1) Upstream the power generation channel (before the anode 90° turn), since the velocity direction of the upstream gas is mainly in the Z-direction rather than the R direction, the directions of the velocity and external magnetic field are basically on the same axis (both are in the z-direction), so $\mathbf{u}\times\mathbf{B}_z \approx 0$, and the effective tangential current density $\mathbf{j}_\theta$ cannot be generated, and the electromagnetic force $\mathbf{j}_\theta \times \mathbf{B}_z$ is also close to zero. Under this condition, the flow characteristics corresponding to no external magnetic field and with an external magnetic field are basically the same. Therefore, applying an external magnetic field does not affect the upstream seed distribution of the power generation channel.

(2) For the effective section of the power generation channel (from the anode inlet to the cathode, including part of the relaxation area), the velocity direction of the gas is the R-direction. If there is an external magnetic field, according to Faraday's law of electromagnetic induction, a large tangential current density $\mathbf{j}_\theta$ will be generated between the anode and the cathode, which will generate an electromagnetic force $\mathbf{j}_\theta \times \mathbf{B}_z$ in the opposite direction to the flow velocity, thus hindering the gas flow. In this case, the flow field will change, which results in the increase in temperature of the effective section, the decrease of the gas Mach number, the change in the location and intensity of the vortex/boundary layer separation, etc. Since the seed mole fraction has a high correlation with the anode inlet state of the power generation channel and the flow field streamlines, the seed distribution will be affected by the flow field and change. The possible results are, if compared with the case without a magnetic field, the non-uniformity coefficient of the seed fraction under an external magnetic field decreases and the spatial distribution is more uniform. However, the seed mass flow rate is limited by the upstream dispersion process, and the average seed fraction is basically at the same level compared with the case without a magnetic field.

The fluid momentum equation and the energy equation with a magnetic field are (which are reflected in the droplet dispersion model and MHD model):

$$\frac{\partial}{\partial t}(\rho\mathbf{u}) + \nabla\cdot(\rho\mathbf{u}\mathbf{u}) = -\nabla p + \nabla\cdot\overline{\tau} + \mathbf{F}_{\mathrm{p}} + \underline{\underline{\mathbf{j}\times\mathbf{B}}}, \tag{17}$$

$$\frac{\partial}{\partial t}(\rho E) + \nabla\cdot(\mathbf{u}(\rho E + p)) = \nabla\cdot(k_{\mathrm{eff}}\nabla T) - Q + \underline{\underline{\mathbf{j}\cdot\mathbf{E}}}. \tag{18}$$

The Smagorinsky model and its versions in large eddy simulation techniques can be used to simulate a high Reynolds number turbulence under a magnetic field.

Considering the condition of complete ionization of Cs, the electrical conductivity of the Ar-Cs non-equilibrium plasma $\sigma_0 \approx 500\,\mathrm{S/m}$. Meanwhile, the maximum velocity of the effective section of the power generation channel $u_0 \approx 1000\,\mathrm{m/s}$. The characteristic scale of plasma $L_0 \approx 70\,\mathrm{mm}$. The magnetic permeability inside the material is approximately the vacuum magnetic permeability $\mu_0 = 4\pi\times10^{-7}\,\mathrm{H/m}$. Therefore, the magnetic Reynolds number of this model Rm can be calculated according to the following equation:

$$\mathrm{Rm} = \mu_0\sigma_0 u_0 L_0 = 0.0440 \ll 1. \tag{19}$$

The following assumptions can be made: (i) due to the absence of high-frequency changes, the displacement current term is ignored; (ii) the electrical neutrality of plasma is always maintained, (iii) due to the magnetic Reynolds number being much smaller than unity, the influence of the induced magnetic field on the external magnetic field is ignored, (iv) consider the steady-state field and ignore the time partial derivative term of the equation. The Maxwell equation can degenerate into the following form:

$$\nabla \times \mathbf{E} = 0, \tag{20}$$

$$\nabla \cdot \mathbf{j} = 0. \tag{21}$$

For disk MHD generators, there exists a generalized Ohm's law as

$$\mathbf{j} + \frac{\beta}{|\mathbf{B}|}\mathbf{j} \times \mathbf{B} = \sigma(\mathbf{E} + \mathbf{u} \times \mathbf{B}). \tag{22}$$

In view of the above equations, a method is proposed in this section, which is to perform a coupling analysis of the MHD model and droplet dispersion model for the effective section of the power generation channel to calculate the distribution of seeds in the effective section under an external magnetic field more accurately. The calculation process is displayed in Fig. 9. First, the initial spatial distribution of the seed fraction $sf^{(0)}$ is calculated under the condition of no electromagnetic force; the seed fraction distribution is substituted into the magnetohydrodynamic model to calculate the current density j and electromagnetic force density $\mathbf{j} \times \mathbf{B}$; then the electromagnetic force density $\mathbf{j} \times \mathbf{B}$ is used as the source term of the droplet dispersion model and substituted into the calculation to obtain a new seed distribution $sf^{(1)}$. The above process is repeated and iterative calculations are continued to determine the final distribution of seed fractions. The plasma flow described by the coupled model can be solved using the k-ε turbulence model [7]. The time step of the MHD model is small (related to the relaxation time of plasma, ns level), whereas the time step of the droplet dispersion model is larger (μs level to ms level), requiring separate solvers.

It should be noted that the above analysis is for gaseous argon-cesium plasma, and the influence of cesium droplets is ignored in the model. In fact, the content of cesium droplets in the power generation channel is less than that of gaseous cesium, but it may affect the collision recombination process of argon cesium plasma, so it needs to be studied in more detail in subsequent research. Moreover, there are difficulties in physically modeling cesium droplets in MHD models because the shape of the cesium droplets is spherical and its diameter becomes smaller ($< 30\,\mu$m) after the cesium is partially vaporized. In comparison, the mesh scale of the MHD model used for calculation is relatively coarse (50–100 μm), making it difficult to model the gas-liquid two-phase interface and to calculate the distribution of the electric field and current density inside cesium droplets. If it is necessary to study the role of cesium droplets in MHD models, a feasible approach is to propose a new plasma electrical conductivity equivalent model to determine the influence of cesium droplets on electrical conductivity.

3. Conclusions.

A three-dimensional numerical simulation was carried out for the flow channel of an inert gas disk MHD generator containing a seed system injection ring and a mixing chamber. The effect of different inlet swirl angles on the mixing of alkali metal seeds and argon main gas flow was studied, and the following conclusions were drawn.

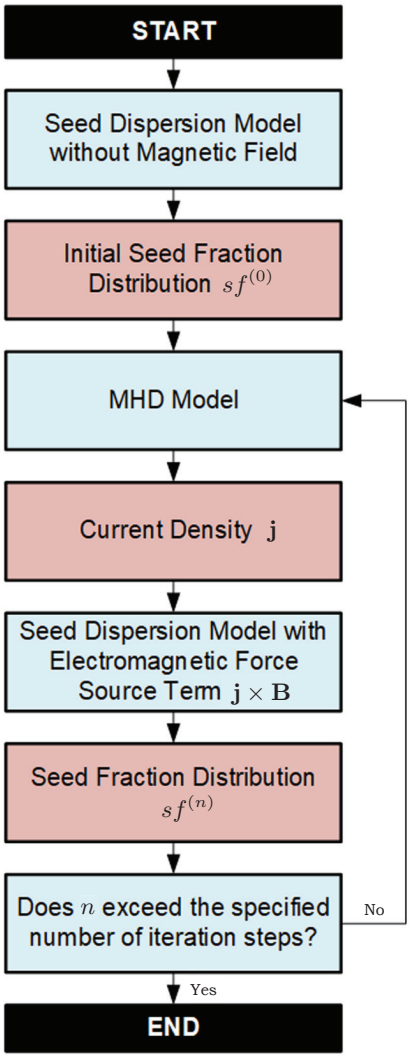

Fig. 9. Coupled solution flowchart of the MHD model and droplet dispersion model.

(1) As the inlet swirl angle increases, due to the centrifugal phenomenon of the cesium droplets, the average seed mole fraction upstream of the power generation channel gradually decreases, and the sudden increase range gradually decreases.

(2) As the inlet swirl angle increases, the seed fraction of gaseous cesium shows an overall decreasing trend in the power generation channel. The spatial distribution patterns of seeds under the conditions of no swirl, small swirl angle and large swirl angle are different: The overall level of the irrotational flow seed fraction is high, and the seed fraction is distributed in a "low level with a negative z value and in a high level with a positive z value". The overall level of seed fractions at small swirl angles is low, and the seed fraction is distributed in a "high level with a negative z value and in a low level with a positive z value". The overall level of the seed fraction for large swirl angles is

low, and the seed fraction is relatively evenly distributed in the Z-direction. The study also showed that the seed fraction of gaseous cesium is controlled by the argon gas flow. The nephogram image results show that the gaseous cesium seed fraction contours have a high correlation with the gas flow streamlines.

(3) As the inlet swirl angle increases, the uneven coefficient of gaseous cesium decreases and the uniformity of the cesium seeds in the effective section of the power generation channel increases, accordingly. However, when the swirl angle increases to a certain value, the uniformity of the cesium seeds in the effective section of the power generation channel will remain basically unchanged.

(4) The plasma ionization characteristics at the entrance of the power generation channel are closely related to the size of the seed fraction. The uneven distribution of seeds in the Z-direction will lead to the uneven spatial distribution of the electron number density and conductivity at the anode inlet. Under the non-rotational flow conditions, the overall level of the electron number density and conductivity is high, with a "low level with a negative zz value and high level with a positive z value" distribution in the Z-direction. Under the condition of inlet swirl, the overall level of the electron number density and conductivity is low, with a "high level with a negative z value and low level with a positive z value" distribution in the Z-direction. The electron number density at the anode inlet generally decreases by about 2–3 orders of magnitude under swirling conditions.

Therefore, the following conclusion can be drawn: when the inlet swirl angle is zero, the electrical conductivity level is highest, and the overall level of the seed fraction in the channel is highest. The optimal inlet swirl angle of the main gas flow is zero.

The simulation has preliminarily confirmed the influence of the inlet swirl flow on the gasification and mixing of cesium seeds. At the same time, the numerical simulation also provides a certain reference for the optimization of seed fraction control methods for the future inert gas plasma MHD generators.

References

[1] T.M. Marinchenko, V.M. Zubtsov. *High Temperature*, vol. 40 (2002), no. 3, pp. 469–476.

[2] T. Murakami, H. Kobayashi, S. Kabashima. *Electrical Engineering in Japan*, 1999.

[3] M. Tanaka, Y. Okuno. *Electrical Engineering in Japan*, vol. 197 (2016), no. 2, pp. 33–40.

[4] L.I. Yiwen, L.I. Yinghong, L.U. Haoyu *et al.* *Chinese Journal of Aeronautics*, vol. 24 (2011), no. 006, pp. 701–708.

[5] T. Murakami, Y. Okuno. *Journal of Physics D Applied Physics*, vol. 41 (2008), no. 12, pp. 125212.

[6] T. Murakami, Y. Okuno, H. Yamasaki. *IEEE Trans Plasma*, vol. 32 (2004), no. 5, pp. 1886–1892.

[7] X.Q. Yuan, T.Z. Zhao, W.K. Guo *et al.* *International Journal of Modern Physics E*, vol. 14 (2005), no. 02, pp. 225–238.

Received 06.01.2024